Journal of Materials Chemistry A

RSC Publishing

PAPER

View Article Online
View Journal | View Issue

Cite this: *J. Mater. Chem. A*, 2013, **1**, 273

Controlled synthesis of hierarchical graphene-wrapped TiO_2@Co_3O_4 coaxial nanobelt arrays for high-performance lithium storage†

Yongsong Luo,‡[abg] Jingshan Luo,‡[a] Weiwei Zhou,[a] Xiaoying Qi,[c] Hua Zhang,[c] Denis Y. W. Yu,[b] Chang Ming Li,[de] Hong Jin Fan[ab] and Ting Yu*[abf]

Received 24th August 2012
Accepted 12th September 2012

DOI: 10.1039/c2ta00064d

www.rsc.org/MaterialsA

As one of the most important research areas in lithium-ion batteries (LIBs), well-designed nanostructures have been regarded as key for solving problems such as lithium ion diffusion, the collection and transport of electrons, and the large volume changes during cycling processes. Here, hierarchical graphene-wrapped TiO_2@Co_3O_4 coaxial nanobelt arrays (G-TiO_2@Co_3O_4 NBs) have been fabricated and further investigated as the electrode materials for LIBs. The results show that the yielded G-TiO_2@Co_3O_4 NBs possess a high reversible capacity, an outstanding cycling performance, and superior rate capability compared to TiO_2 and TiO_2@Co_3O_4 nanobelt array (TiO_2@Co_3O_4 NBs) electrodes. The core–shell TiO_2@Co_3O_4 NBs may contain many cavities and provide more extra spaces for lithium ion storage. The introduction of graphene into nanocomposite electrodes is favorable for increasing their electrical conductivity and flexibility. The integration of hierarchical core–shell nanobelt arrays and conducting graphene may induce a positive synergistic effect and contribute to the enhanced electrochemical performances of the electrode. The fabrication strategy presented here is facile, cost-effective, and can offer a new pathway for large-scale energy storage device applications.

1 Introduction

With the rapid depletion of fossil fuels and increasingly worsened environmental pollution caused by vast fossil-fuel consumption, scientists worldwide are searching for renewable and clean energy sources to replace traditional fossil fuels that can enable the sustainable development of our economy and society. However, exploitation of alternative and green energy sources requires the efficient support of energy storage/conversion devices that can compensate for their intermittent characteristics. In this context, lithium ion batteries (LIBs) have attracted worldwide concern and increasing research interest over the past decade due to the fact that they can continuously and efficiently store electrochemical energy.[1–3]

Currently, the ever-growing market demand for high energy density, high power density, good safety, and long cycle life has stimulated numerous research efforts aimed at the development of new high performance electrode materials for LIBs.[4–7] Transition metal oxides (M_xO_y, M = Fe, Co, V, *etc.*) have long been focused on as anode materials for LIBs due to their high electrochemical capacities compared to carbonaceous materials. However, an intrinsic disadvantage associated with drastic volume variation makes these metal oxide based anodes suffer from rapid capacity loss, especially at high charge–discharge rates upon cycling which thereby limits their potential use as electrodes.[8–11] Among diverse metal oxides, titania has received special interest as an anode material for LIBs because it is not only a fast and low voltage insertion host for Li, but is also an abundant, low cost and environmentally benign material with a very low volume change.[12,13] Unfortunately, the poor electrical transport of titania constitutes a major obstacle for its practical application in lithium storage given that a high overpotential is commonly applied during the cycling processes and thus dramatically diminishes its rate performances.[14,15] Thus, developing new synthetic strategies to fabricate high performance metal oxide electrode materials with satisfactory

[a]*Division of Physics and Applied Physics, School of Physical and Mathematical Sciences, Nanyang Technological University, 637371, Singapore. E-mail: yuting@ntu.edu.sg*

[b]*Energy Research Institute at Nanyang Technological University (ERIAN), 639789 Singapore*

[c]*School of Materials Science and Engineering, Nanyang Technological University, 639798, Singapore*

[d]*Institute for Clean Energy and Advanced Materials, Southwest University, Chongqing 400700, P. R. China*

[e]*Division of Bioengineering, School of Chemical and Biomedical Engineering, Nanyang Technological University, 637371, Singapore*

[f]*Department of Physics, Faculty of Science, National University of Singapore, 117542 Singapore*

[g]*School of Physics and Electronic Engineering, Xinyang Normal University, Xinyang 464000, P. R. China*

† Electronic supplementary information (ESI) available. See DOI: 10.1039/c2ta00064d

‡ These authors contributed equally to this work.

high-rate capability and high specific capacity is still a great challenge. To overcome the above-mentioned issues, various metal oxide based nanocomposites with different geometrical attributes, morphological forms, and microarchitectures have been employed as anode materials for LIBs.[5,16,17] For instance, TiO_2–RuO_2, Co_3O_4–C, and MoO_2–graphene nanocomposites have been demonstrated with improved Li ion insertion performance since they use conductive additives to interlink the host nanostructures.[14,18–22] Moreover, hierarchical nanostructures have also aroused much interest in a variety of fields because of their extraordinarily high active surface/interface and robust stability.[23–29] Electrode materials with a hierarchical nanoarchitecture can not only provide multiple large contact areas, but also allow fast Li ion transport between the electrolyte and the electrode.

In this work, we report the synthesis of hierarchical graphene-wrapped TiO_2@Co_3O_4 nanobelt arrays (G-TiO_2@Co_3O_4 NBs) as anode materials for LIB applications. This hierarchical structure is expected to manifest greatly improved electrochemical performance due to the integration of many advantages. Firstly, owing to its large surface area, good structural flexibility, and superior electrical conductivity, graphene can effectively buffer the large volume expansion/contraction and improve the electrical contact of the active materials with current collectors during charge–discharge processes.[21,30–34] Secondly, both the core and shell materials are relatively abundant, low cost, and environmentally benign. In particular, the Co_3O_4 nanoparticles grafted on the TiO_2 backbone are beneficial for enhancing the electrochemical capacity and cycling stability of the electrode due to the high theoretical capacity of the Co_3O_4 shell and the low volume change of the TiO_2 core. Thirdly, well-ordered nanostructure arrays grown directly on current collectors show an improved performance, which is induced by the good contact of the active materials and adhesion with the current collector, as well as good strain accommodation.[35] This well engineered hierarchical nanostructure not only provides a large interfacial area for fast lithium insertion/extraction but also reduces the diffusion pathways for electronic and ionic transport. As a consequence, we have tested the hierarchical G-TiO_2@Co_3O_4 NBs as potential anode materials for LIBs, exhibiting good rate capability, excellent cycle performance, and highly reversible capacity.

2 Experimental

Synthesis of TiO_2 nanobelt arrays (TiO_2 NBs)

The fabrication process of the TiO_2 NBs on Ti foils was as follows:[36] first, the Ti foils (99.7% purity, 0.25 mm thickness, Sigma-Aldrich) were cut into small pieces (1.5 × 4.0 cm) and sonicated in acetone, ethanol, and deionized water for 10 min, respectively. Then they were put into 40 mL of 5 M NaOH aqueous solution in a 50 mL Teflon-lined autoclave. The autoclave was kept at 200 °C for 24 h. After cooling down naturally to room temperature, the samples were washed with deionized water several times and dried in a dry cabinet. Then the samples were immersed in 1.2 M HCl solution for 2 h in order to exchange the Na^+ with H^+. Finally, the as-prepared samples were annealed at 450 °C for 1 h in an electronic furnace.

Synthesis of TiO_2@Co_3O_4 nanobelt arrays (TiO_2@Co_3O_4 NBs)

TiO_2@Co_3O_4 NBs were prepared using a hydrothermal growth method.[37] In a typical synthesis procedure, 0.1 g of $Co(NO_3)_2 \cdot 6H_2O$, 0.5 g of $CO(NH_2)_2$, and 0.37 g of NH_4F were added to 40 mL of water and stirred at room temperature for 10 min. The homogeneous solution was transferred into a 50 mL Teflon-lined autoclave. In the meantime, a piece of TiO_2 NBs on Ti foil was introduced into the autoclave. Then the autoclave was sealed and maintained at 120 °C for 5 h, and allowed to cool to ambient temperature naturally. Finally, the resulting precursor was repeatedly washed with distilled water, then dried at 60 °C for 3 h, followed by a calcination treatment in air at 400 °C for 4 h.

Synthesis of G-TiO_2@Co_3O_4 NBs

Graphene oxide (GO) was prepared using a modified Hummers method.[38] To fabricate graphene-wrapped TiO_2@Co_3O_4 NBs, a general strategy can be achieved by immersing the TiO_2@Co_3O_4 NBs sequentially into the following three solutions for varied durations at room temperature.[39] Typically, a piece of substrate covered with the TiO_2@Co_3O_4 NBs was first immersed into a 1 g L^{-1} poly(allylamine hydrochloride) (PAH) solution for 1 h, followed by immersing the 0.2 g L^{-1} GO dispersion for 5 h. Then, the sample was transferred into hydrazine (N_2H_4, 98%) solution for 0.5 h. Finally, the sample was removed, washed with deionized water, and dried at 60 °C to obtain the G-TiO_2@Co_3O_4 NBs.

Characterization

The phase purity of the products was characterized by X-ray powder diffraction (XRD) using an X-ray diffractometer with Cu Kα radiation (λ = 1.5418 Å). Scanning electron microscopy (SEM) images were obtained using a JEOL JSM 6700F microscope (Japan). Transmission electron microscopy (TEM) and high-resolution TEM (HRTEM) observations were carried out on a JEOL JEM-2010 instrument in bright field and on a HRTEM JEM-2010FEF instrument (operated at 200 kV). Raman spectroscopy was carried out using a WITEC CRM200 Raman system equipped with a 532 nm laser source and a 100× objective lens. X-Ray photoelectron spectroscopy (XPS) spectra were measured on a Perkin-Elmer model PHI 5600 XPS system with a resolution of 0.3–0.5 eV from a monochromated aluminum anode X-ray source.

Electrochemical evaluation

The Swagelok-type batteries were assembled in an Ar-filled glovebox (Mbraun, Unilab, Germany) by directly using the G-TiO_2@Co_3O_4 NBs on Ti foils ($m_{G+TiO2+Co3O4}$ = 0.006 g; $m_G \approx$ 0.000 g, m_{TiO2} = 0.004 g, m_{Co3O4} = 0.002 g) as the anode materials, a Li-metal circular foil (0.59 mm thick) as the counter and reference electrodes, a microporous polypropylene membrane as the separator, and a 1 M solution of $LiPF_6$ in

ethylene carbonate (EC) and diethyl carbonate (DEC) (1 : 1 by volume) as the electrolyte. The cell was aged for 15 h before measurement. The discharge–charge cycling was performed at room temperature by using a multichannel battery tester (model SCN, USA).

3 Results and discussion

A schematic illustration and optical images of the G-TiO_2@Co_3O_4 NBs on Ti foil are displayed in Fig. 1. The whole process involves three steps (Fig. 1a): first, TiO_2 NBs were synthesized through ion exchange from the titanate precursor nanobelt arrays. Then, a Co_3O_4 nanoparticle layer was grown on the surface of the TiO_2 NBs *via* a hydrothermal process. Finally, the as-obtained TiO_2@Co_3O_4 NBs were coated with graphene oxide and further reduced by hydrazine hydrate in solution, producing the hierarchical G-TiO_2@Co_3O_4 NBs. Fig. 1b–d show optical images of the TiO_2 NBs, TiO_2@Co_3O_4 NBs, and integrated G-TiO_2@Co_3O_4 NBs on a current collector, respectively. It can be seen that the Ti foil surface turned completely grey white after the initial growth of TiO_2 NBs. Furthermore, the TiO_2/Ti substrate was observed to become dark black after the deposition of Co_3O_4, indicating the formation of a Co_3O_4 layer on the surface of the TiO_2 NBs. Eventually, the formation of G-TiO_2@Co_3O_4 NBs still emerged as dark black owing to an ultrathin layer of graphene sheets covering the surface of the TiO_2@Co_3O_4 NBs. Typical XRD patterns of the as-prepared TiO_2, TiO_2@Co_3O_4 and G-TiO_2@Co_3O_4 NBs are distinctly demonstrated in Fig. 2a–c. Besides the peaks originating from the Ti substrate, almost all the identified peaks can be indexed to anatase TiO_2 (JCPDS card no. 21-1272) and cubic spinel Co_3O_4 (JCPDS card no. 42-1467).[40,41] Moreover, the weak peak centered at ~23° indicates the existence of amorphous carbon (Fig. 2c).[42,43]

SEM images of the TiO_2 and TiO_2@Co_3O_4 NBs are shown in Fig. 3. Evidently, the top-view and cross-sectional SEM images of the as-obtained products show well-aligned TiO_2 NBs

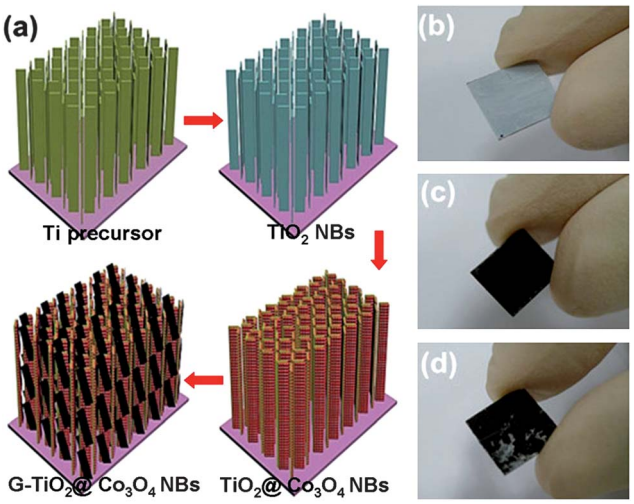

Fig. 1 (a) Schematic representation for the formation processes of G-TiO_2@Co_3O_4 NBs; (b–d) optical images of TiO_2, TiO_2@Co_3O_4 and G-TiO_2@Co_3O_4 NBs.

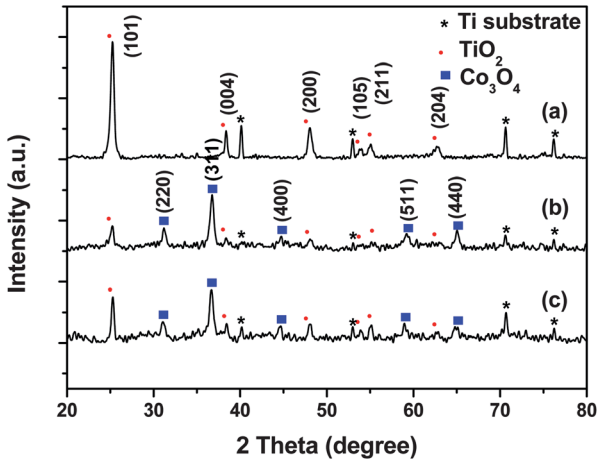

Fig. 2 XRD patterns of as-prepared TiO_2 NBs (curve a); TiO_2@Co_3O_4 NBs (curve b); G-TiO_2@Co_3O_4 NBs (curve c).

(Fig. 3a–c). Close observation reveals that an individual TiO_2 nanobelt is typically about 8–11 μm in length, ~500 nm in width, and ~20 nm in thickness. When this TiO_2 nanobelt experienced a hydrothermal process for Co_3O_4 growth without

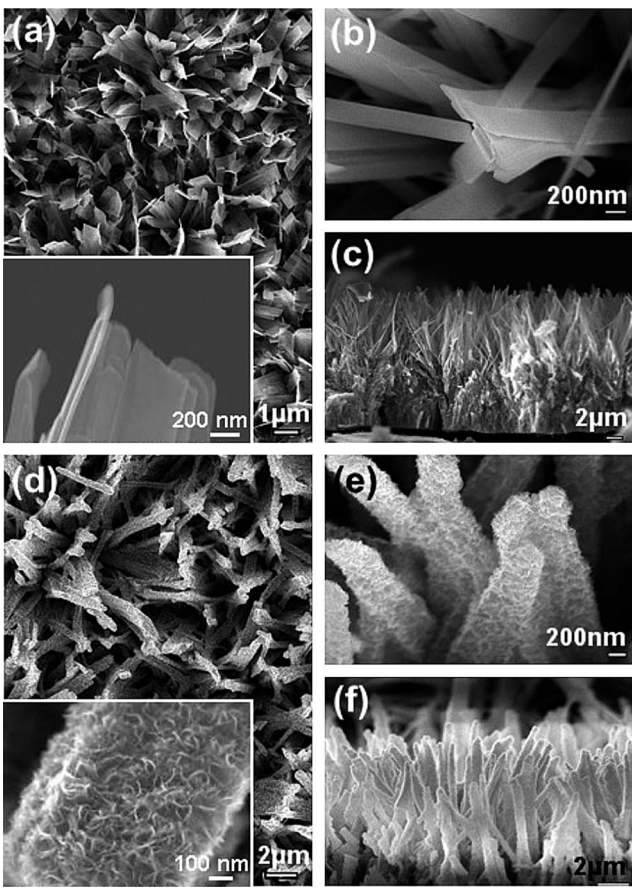

Fig. 3 (a and b) Low-magnification and enlarged SEM images of TiO_2 NBs; (c) cross-sectional SEM image of TiO_2 NBs; (d and e) low-magnification and enlarged SEM images of TiO_2@Co_3O_4 NBs; (f) cross-sectional SEM image of TiO_2@Co_3O_4 NBs.

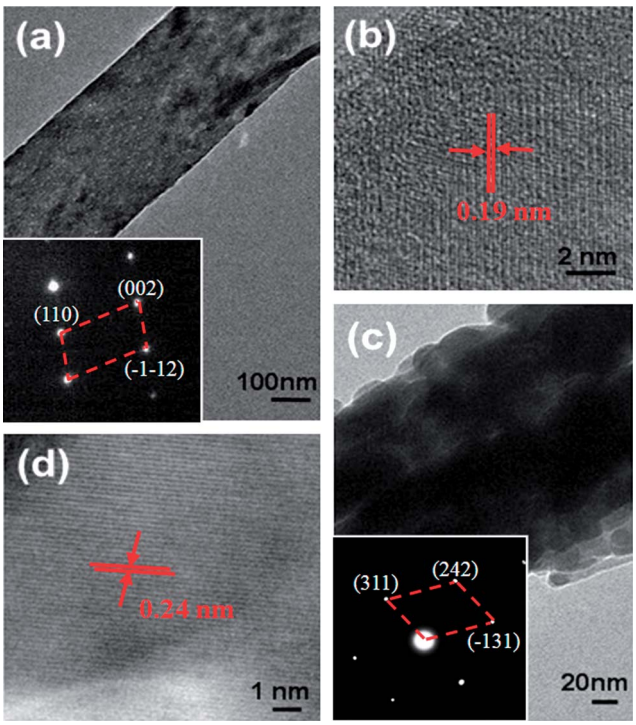

Fig. 4 (a and b) Low-magnification and high-magnification TEM images of TiO_2 nanobelt; (c and d) low-magnification and high-magnification TEM images of TiO_2@Co_3O_4 nanobelt; the insets of (a) and (c) are the corresponding SAED patterns from TiO_2 and TiO_2@Co_3O_4 nanobelts.

any additional growth catalysts, its surface was remarkably covered with a layer of dense Co_3O_4 nanoflakes as shown in Fig. 3d–f. Similarly, the morphology of the TiO_2@Co_3O_4 composite displays a belt-like shape but a rough surface. The structures of the nanobelts were further investigated by TEM. Fig. 4a shows the TEM image of an individual TiO_2 nanobelt, and its corresponding HRTEM image taken near the edge is shown in Fig. 4b. A lattice spacing of 0.19 nm is recognized and can be ascribed to the (200) planes of anatase TiO_2. The selected area electron diffraction (SAED) pattern of the TiO_2 nanobelt shows a set of well-defined spots, indicative of single-crystallinity. A TEM image of the Co_3O_4 nanostructures on the surface of a TiO_2 nanobelt is also shown in Fig. 4c. From this image, a flake-like Co_3O_4 nanoshell was observed, fully covering the TiO_2 nanobelt surface. In addition, SAED was performed to investigate the crystalline characteristics of the TiO_2@Co_3O_4 nanobelt, based on the selected area shown in the inset of Fig. 4c. Clear lattice fringes were also observed (Fig. 4d), further demonstrating the superior crystal quality of the TiO_2@Co_3O_4 NBs. Fig. 5a–c show the representative SEM images for the G-TiO_2@Co_3O_4 NB product at different magnifications. No significant change in the morphology was observed in comparison to the TiO_2@Co_3O_4 NBs. Further observation indicates that the TiO_2@Co_3O_4 NBs are wrapped by the graphene layers and assembled into hierarchical nanoarchitectures. To provide further insight into the morphology and structure of the resulting G-TiO_2@Co_3O_4 NBs, TEM investigations were carried out. Fig. 5d and e show a portion of the G-TiO_2@Co_3O_4 nanobelt hierarchical nanostructure. Across the core–shell structure, it is clearly observed that the ultrathin graphene is located around the TiO_2@Co_3O_4 nanobelt surface. Fig. 5f shows a HRTEM image taken from the edge of an individual G-TiO_2@Co_3O_4 nanobelt; the interplanar spacing of ~0.34 nm corresponds to the separation between the (002) lattice planes of graphite. This demonstrates that the TiO_2@Co_3O_4 nanobelt assemblies are well wrapped by the ultrathin layer of graphene sheets.

To make sure the entire arrays are converted into G-TiO_2@Co_3O_4 NBs, the compositions of the G-TiO_2@Co_3O_4 NBs were characterized by Raman spectroscopy. The existence of pure phases of TiO_2 and Co_3O_4 are clearly reflected in the Raman spectra (Fig. 6).[44,45] Moreover, the characteristic D band at ~1345 cm^{-1} and G band at ~1586 cm^{-1} are observed for the G-TiO_2@Co_3O_4 NBs. The G-TiO_2@Co_3O_4 NBs are strongly anchored onto the Ti foil with good adhesion. The robust mechanical adhesion is manifested by the fact that no material

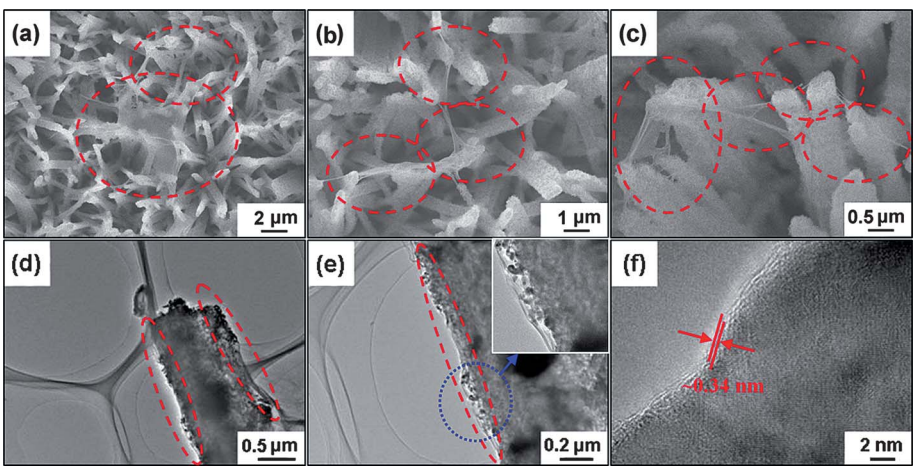

Fig. 5 (a–c) SEM images of G-TiO_2@Co_3O_4 NBs at different magnifications; (d and e) low-magnification and enlarged TEM images of an individual G-TiO_2@Co_3O_4 nanobelt; (f) HRTEM image of the edge part of one G-TiO_2@Co_3O_4 nanobelt.

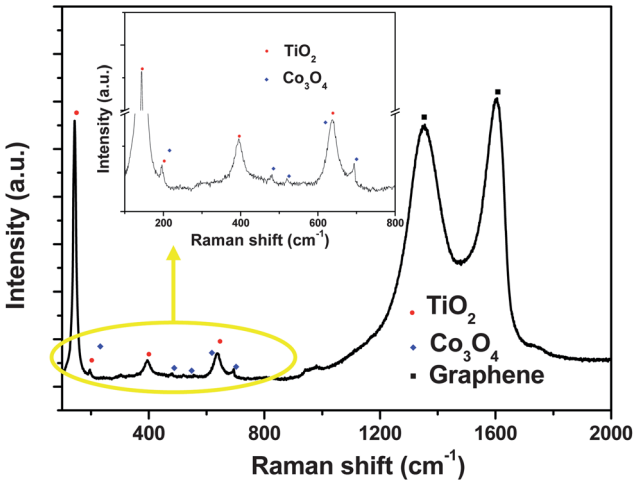

Fig. 6 Raman spectrum of G-TiO_2@Co_3O_4 nanobelt arrays. The inset is the magnification of part of the Raman spectrum.

loss occurred after sonication in solution for several minutes, which is very promising for improving the electrochemical performance of the electrode. For comparison, the significant compositional changes during the chemical processing from TiO_2 to TiO_2@Co_3O_4 NBs are also characterized by Raman spectroscopy (Fig. S1, see ESI†). To estimate the surface electronic state and the composition of the final products, we carried out an XPS study (Fig. 7). The high resolution C 1s spectrum of the G-TiO_2@Co_3O_4 NBs is shown in Fig. 7a. It can be decomposed into four peaks at 284.6, 286.1, 287.4, and 289 eV, respectively.[46] These components can be assigned to C from non-oxygenated carbon (CC), COC/COH, a carbonyl group (CO), and a COOH group. The strong C 1s peak (284.6 eV) is related to graphitic carbon in graphene, while the weaker ones from the oxygenated indicate that a certain degree of deoxygenation process accompanies the reduction of graphene oxide.[22] The deconvoluted peaks (Fig. 7b) of the O 1s spectrum are also resolved into four components, centered at 530, 531.2, 533, and 534.7 eV, respectively. The low binding energy component observed at 530 eV is attributed to the O^{2-} forming oxides with titanium and cobalt, while the latter three peaks are assigned to OH^-, C–O and O–C=O, and H_2O, respectively.[47–49] Fig. 7c presents the XPS spectra of Ti 2p doublet peaks; the binding energies of Ti $2p_{1/2}$ and Ti $2p_{3/2}$ were observed at approximately 466 eV and 460 eV, respectively, which is typical of Ti^{4+} in an octahedral environment.[50] Similarly, the core level spectra of Co 2p were curve fitted and are shown in Fig. 7d. The spectrum shows two major peaks at 779.8 and 795.2 eV, assigned to the Co $2p_{3/2}$ and Co $2p_{1/2}$ peaks, respectively. The absence of prominent shake-up satellite peaks in the Co 2p spectra further suggests the formation of the Co_3O_4 phase.[51,52]

Discharge–charge measurements for the G-TiO_2@Co_3O_4 NBs were carried out in the potential range of 5 mV to 3.0 V (*vs.* Li) at a current density of 100 mA g^{-1} up to 200 cycles at ambient temperature. The voltage *versus* capacity profiles are shown in Fig. 8a. In the discharge curve of the first cycle, there are two

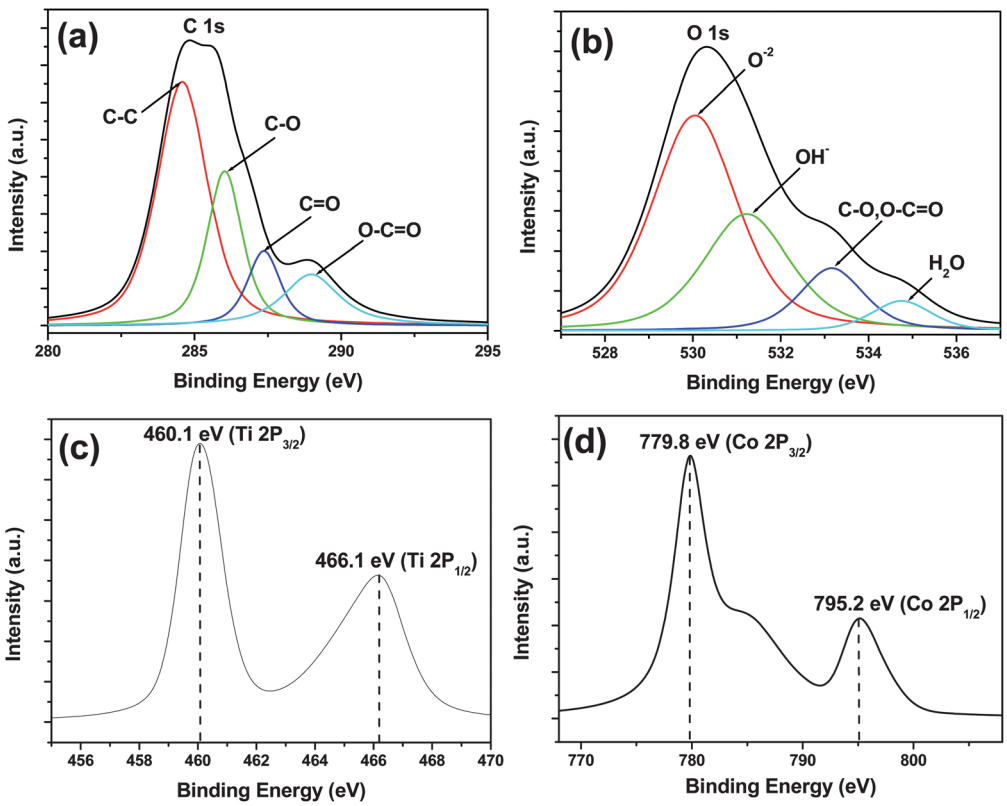

Fig. 7 XPS spectra of (a) C 1s, (b) O 1s, (c) Ti 2p and (d) Co 2p regions of G-TiO_2@Co_3O_4 nanobelt arrays.

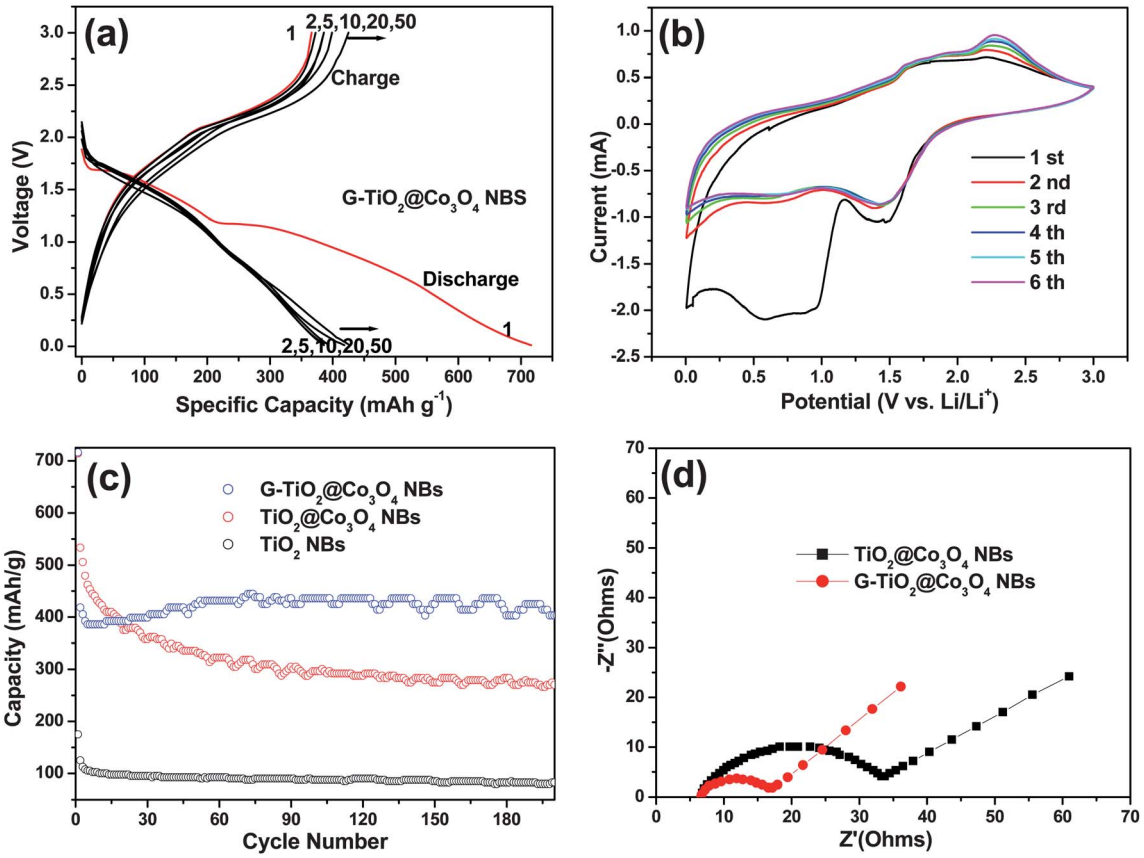

Fig. 8 (a) Galvanostatic discharge–charge profiles of G-TiO_2@Co_3O_4 NBs at a constant current density of 100 mA g^{-1}; (b) CV curve of G-TiO_2@Co_3O_4 NB anode at 0.5 mV s^{-1} scanning rate; (c) cycling performance of the anodes at a constant current density of 100 mA g^{-1}; (d) electrochemical impedance spectra of TiO_2@Co_3O_4 and G-TiO_2@Co_3O_4 NBs after 1st cycle.

obvious voltage plateaus (~1.7 and ~1.2 V) resulting from the lithium reactions with TiO_2 and Co_3O_4, respectively. The first plateau at ~1.7 V is associated with the phase transition between the tetragonal TiO_2 and orthorhombic Li_xTiO_2 phases.[53–55] The second plateau at ~1.2 V can be ascribed to the initial reduction of Co_3O_4 to metallic cobalt, accompanied by the electrochemical formation of amorphous Li_2O.[56,57] The following sloping region may be related to the formation of a solid electrolyte interphase (SEI) film which can cause irreversible capacity loss. The charge curve shows a broad sloping plateau (1.4–2.1 V) due to reversible reactions. It is also observed that the initial discharge and charge capacities for the G-TiO_2@Co_3O_4 NBs are ~713 and ~364 mA h g^{-1}, respectively. The initial capacity loss of 48.9% may be mainly attributed to irreversible processes such as the inevitable formation of an SEI film and electrolyte decomposition, which are common to most anode materials.[58] Moreover, the voltage-capacity trace of the TiO_2 and TiO_2@Co_3O_4 NBs were also recorded for comparison (Fig. S2†). The results indicate that the first discharge capacity of ~713 mA h g^{-1} for the G-TiO_2@Co_3O_4 NBs is higher than those of TiO_2@Co_3O_4 NBs (~709 mA h g^{-1}) and TiO_2 NBs (~174.5 mA h g^{-1}). The reversible capacity for the G-TiO_2@Co_3O_4 NBs is further observed to gradually increases up to the 50th cycle. Fig. 8b shows the cyclic voltammetry (CV) curves of the G-TiO_2@Co_3O_4 NB electrode at a scan rate of 0.5 mV s^{-1} over the range of 0.005–3.0 V. In the first cycle, two pronounced reduction peaks are observed at ~0.8 V and ~1.5 V, which can be attributed to the formation of Li_2O, as well as the SEI film.[7,41] The subsequent well-defined oxidation peaks are observed at ~1.6 V and ~2.2 V, indicating the extraction of Li^+ in the electrode materials.[59,60] These results nearly coincide with the voltage plateaus in the galvanostatic discharge–charge curve (Fig. 8a). The second and onward CV curves remain steady, indicating highly reversible redox behaviour. This is consistent with its good cycling performance, as discussed below. Moreover, cyclic voltammograms were also investigated on the cells with TiO_2 and TiO_2@Co_3O_4 NBs for comparison (Fig. S3†).

The capacity *versus* cycle number plot is shown in Fig. 8c. As can be seen, it is evident that the G-TiO_2@Co_3O_4 NB electrode exhibits exceptional cyclability. The capacity increases gradually in the first 60 cycles and stabilizes at around ~437 mA h g^{-1} in the subsequent cycles. Although the TiO_2@Co_3O_4 NBs deliver the same capacity as the G-TiO_2@Co_3O_4 NBs in the first cycle, they exhibit drastic capacity fading over the course of the discharge–charge cycles. The capacity difference between the G-TiO_2@Co_3O_4 and TiO_2@Co_3O_4 NBs becomes large upon cycling, implying that the graphene layers on the surface of the TiO_2@Co_3O_4 NBs play an essential role in improving the cyclic performance. Moreover, the capacity enhancement can be mainly attributed to the increased reactive sites of the G-TiO_2@Co_3O_4

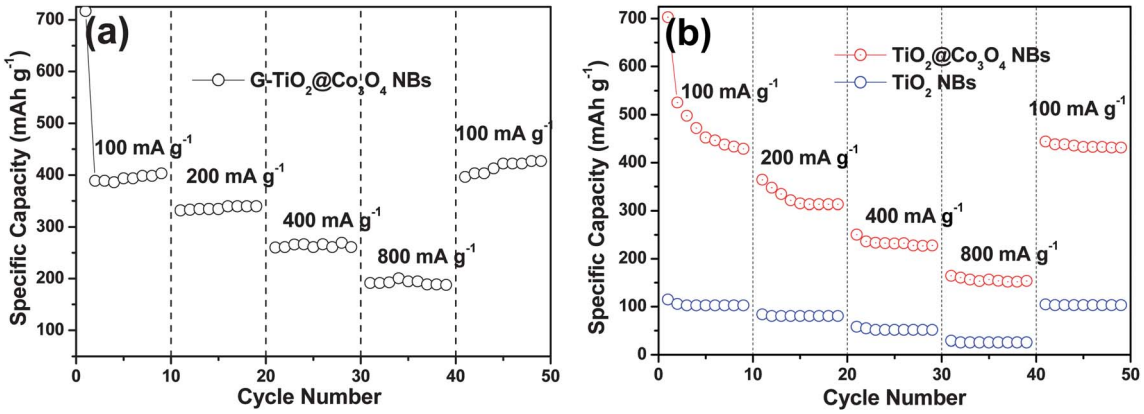

Fig. 9 (a) Reversible capacity *vs.* current density (rate capability) for G-TiO_2@Co_3O_4 NB anode; (b) reversible capacity *vs.* current density (rate capability) for TiO_2 and TiO_2@Co_3O_4 NB anodes.

NBs which have been activated in the subsequent cycling, participating in lithium-ion storage and contributing to the final capacity.[19,39,61] In order to clarify the influence of hybridization on the electrochemical performance of the G-TiO_2@Co_3O_4 NBs, we have calculated the theoretical capacity of the physical mixture of pristine materials. The theoretical capacity (C) of the G-TiO_2@Co_3O_4 NBs is calculated as follows:[62] $C_{\text{theoretical}} = C_{\text{Graphite}} \times \%_{\text{mass of CTs}} + C_{TiO_2} \times \%_{\text{mass of } TiO_2} + C_{Co_3O_4} \times \%_{\text{mass of } Fe_2O_3} = 372 \times 0.00 + 335 \times 0.67 + 890 \times 0.33 = 520$ mA h g^{-1}. The above results show that the G-TiO_2@Co_3O_4 NBs can deliver an average capacity of ~437 mA h g^{-1} that is equal to 84% of the theoretical value. However, the capacities of the TiO_2 and TiO_2@Co_3O_4 NBs are only ~89 and ~306 mA h g^{-1}, respectively, at the 90th cycle. Moreover, the first discharge specific capacity of the G-TiO_2@Co_3O_4 NBs is about 713 mA h g^{-1}, which is larger than the theoretically predicted value for G-TiO_2@Co_3O_4 NBs. This phenomenon is attributed to the formation of an SEI layer, generated by the irreversible insertion/deinsertion of Li ions into the host structures or on Li alloying reactions and possible interfacial Li storage.[63–65] For a better understanding of the superior electrochemical performance of the G-TiO_2@Co_3O_4 NBs compared with TiO_2@Co_3O_4 NBs for lithium energy storage, the electrochemical impedance spectroscopy (EIS) was performed with an amplitude of 5.0 mV over the frequency range from 100 kHz to 0.01 Hz (Fig. 8d). The resulting Nyquist plot exhibits two distinct parts, including a semicircle in the high frequency region and a sloped line in the low frequency region, further demonstrating the long-term electrochemical stability of this electrode material. It is worth noting that the diameter of the semicircle for the G-TiO_2@Co_3O_4 NBs (10.5 Ω) is much smaller than that of the TiO_2@Co_3O_4 NBs (28 Ω), which suggests that the G-TiO_2@Co_3O_4 NBs possess lower contact and charge-transfer resistances. This result indicates that the graphene layers wrapped on the TiO_2@Co_3O_4 NBs not only improve the conductivity of the electrode, but also largely enhance the electrochemical activity of the TiO_2@Co_3O_4 NBs during the cycling processes.

In order to better understand the rate performance of the G-TiO_2@Co_3O_4 NBs, the cycling response at continuously variable rates was evaluated (Fig. 9a). All of the electrodes were first cycled at a current density of 100 mA g^{-1}. An irreversible capacity loss during the first cycle is observed for the electrodes, which is presumably due to decomposition of the electrolyte and/or solvent. Remarkably, in the case of the G-TiO_2@Co_3O_4 NBs, the reversible capacities are retained at ~345 and ~204 mA h g^{-1} at 200 and 800 mA g^{-1}, respectively. In contrast, the capacity of the TiO_2@Co_3O_4 NBs decreases to ~313 and ~151 mA g^{-1} under the same testing conditions. After 50 cycles, with the current rate being decreased back to 100 mA g^{-1}, a capacity of ~431 mA h g^{-1} can be recovered for the G-TiO_2@Co_3O_4 NBs. Benefitting from the unique hierarchical structure and the presence of graphene wrapping, the G-TiO_2@Co_3O_4 NBs are able to demonstrate excellent rate performance and cyclability, emphasizing the efficiency of our protocol in improving the electrochemical performance.

4 Conclusions

In summary, we have demonstrated an efficient strategy for the synthesis of well-ordered hierarchical G-TiO_2@Co_3O_4 NBs. The results show that the as-formed hierarchical G-TiO_2@Co_3O_4 NBs exhibit highly reversible capacity, excellent cyclability, and good rate capability as anode materials for LIBs. The unique textural features of the G-TiO_2@Co_3O_4 NBs, including the coaxial core–shell structure, good contact and adhesion of the active materials with the current collector, and the homogeneous dispersion of the graphene layer in each TiO_2@Co_3O_4 nanobelt, lead to this remarkable electrochemical performance. It is expected that the structural design of the electrodes in this work provides a facile protocol to prepare other hierarchical nanostructured electrode materials, thus creating a new opportunity for designing next generation energy storage devices.

Acknowledgements

This work is supported by the Singapore National Research Foundation under NRF RF Award no. NRF-RF2010-07, MOE Tier 2 MOE2009-T2-1-037 and CRP Award no.: NRF-CRP4-2008-03.

Notes and references

1 K. T. Nam, D. W. Kim, P. J. Yoo, C. Y. Chiang, N. Meethong, P. T. Hammond, Y. M. Chiang and A. M. Belcher, *Science*, 2006, **312**, 885.
2 C. K. Chan, H. Peng, G. Liu, K. McIlwrath, X. F. Zhang, R. A. Huggins and Y. Cui, *Nat. Nanotechnol.*, 2008, **3**, 31.
3 K. Kang, Y. S. Meng, J. Breger, C. P. Grey and G. Ceder, *Science*, 2006, **311**, 977.
4 T. H. Han, W. J. Lee, D. H. Lee, J. E. Kim, E.-Y. Choi and S. O. Kim, *Adv. Mater.*, 2010, **22**, 2060.
5 A. S. Arico, P. Bruce, B. Scrosati, J.-M. Tarascon and W. V. Schalkwijk, *Nat. Mater.*, 2005, **4**, 366.
6 Y. Idota, T. Kubota, A. Matsufuji, Y. Maekawa and T. Miyasaka, *Science*, 1997, **276**, 1395.
7 Y. C. Qiu, K. Y. Yang, L. M. Jin, H. Dong and W. S. Li, *ACS Nano*, 2010, **4**, 6515.
8 J. Chen, L. Xu, W. Li and X. Gou, *Adv. Mater.*, 2005, **17**, 582.
9 C. Ban, Z. Wu, D. T. Gillaspie, L. Chen, Y. Yan, J. L. Blackburn and A. C. Dillon, *Adv. Mater.*, 2010, **22**, E145.
10 A. M. Cao, J. S. Hu, H. P. Liang and L. J. Wan, *Angew. Chem., Int. Ed.*, 2005, **44**, 4391.
11 W. J. Lee, J. M. Lee, S. T. Kochuveedu, T. H. Han, H. Y. Jeong, M. Park, J. M. Yun, J. Kwon, K. No, D. H. Kim and S. O. Kim, *ACS Nano*, 2012, **6**, 935.
12 M. M. Rahman, J. Z. Wang, M. F. Hassan, D. Wexler and H. K. Liu, *Adv. Energy Mater.*, 2011, **1**, 212.
13 J. H. Liu, J. S. Chen, X. F. Wei, X. W. Lou and X. W. Liu, *Adv. Mater.*, 2011, **23**, 998.
14 Y. G. Guo, Y. S. Hu, W. Sigle and J. Maier, *Adv. Mater.*, 2007, **19**, 2087.
15 S. B. Yang, X. L. Feng and K. Müllen, *Adv. Mater.*, 2011, **23**, 3575.
16 V. Etacheri, R. Marom, R. Elazari, G. Salitra and D. Aurbach, *Energy Environ. Sci.*, 2011, **4**, 3243.
17 M. V. Reddy, T. Yu, C. H. Sow, Z. X. Shen, C. T. Lim, G. V. S. Rao and B. V. R. Chowdari, *Adv. Funct. Mater.*, 2007, **17**, 2792.
18 S. H. Nam, H. S. Shim, Y. S. Kim, M. A. Dar, J. G. Kim and W. B. Kim, *ACS Appl. Mater. Interfaces*, 2010, **2**, 2046.
19 Y. S. Luo, J. Jiang, W. W. Zhou, H. P. Yang, J. S. Luo, X. Y. Qi, H. Zhang, D. Y. W. Yu, C. M. Li and T. Yu, *J. Mater. Chem.*, 2012, **22**, 8634.
20 F. F. Cao, Y. G. Guo, S. F. Zheng, X. L. Wu, L. Y. Jiang, R. R. Bi, L. J. Wan and J. Maier, *Chem. Mater.*, 2010, **22**, 1908.
21 D. H. Wang, D. W. Choi, J. Li, Z. G. Yang, Z. M. Nie, R. Kou, D. H. Hu, C. M. Wang, L. V. Saraf, J. G. Zhang, I. A. Aksay and J. Liu, *ACS Nano*, 2009, **3**, 907.
22 Y. M. Sun, X. L. Hu, W. Luo and Y. H. Huang, *ACS Nano*, 2011, **5**, 7100.
23 A. Magasinski, P. Dixon, B. Hertzberg, A. Kvit, J. Ayala and G. Yushin, *Nat. Mater.*, 2010, **9**, 353.
24 L. Mai, L. Xu, C. Han, X. Xu, Y. Luo, S. Zhao and Y. Zhao, *Nano Lett.*, 2010, **10**, 4750.
25 J. S. Chen, Y. L. Tan, C. M. Li, Y. L. Cheah, D. Luan, S. Madhavi, F. Y. C. Boey, L. A. Archer and X. W. Lou, *J. Am. Chem. Soc.*, 2010, **132**, 6124.
26 X. S. Fang, L. F. Hu, K. F. Huo, B. Gao, L. J. Zhao, M. Y. Liao, P. K. Chu, Y. Bando and D. Golberg, *Adv. Funct. Mater.*, 2011, **21**, 3907.
27 F. Sun, J. C. Yu and X. Wang, *Chem. Mater.*, 2006, **18**, 3774.
28 J. Jiang, J. P. Liu, W. W. Zhou, J. H. Zhu, X. T. Huang, X. Y. Qi, H. Zhang and T. Yu, *Energy Environ. Sci.*, 2011, **4**, 5000.
29 Y. Y. Lu, F. Zhang, Y. Q. Dou, Y. P. Zhai, J. X. Wang, H. J. Liu, Y. Y. Xia, B. Tu and D. Y. Zhao, *J. Mater. Chem.*, 2012, **22**, 93.
30 X. Wang, X. Zhou, K. Yao, J. Zhang and Z. Liu, *Carbon*, 2011, **49**, 133.
31 G. Zhou, D. W. Wang, F. Li, L. Zhang, N. Li, Z. S. Wu, L. Wen, G. Q. Lu and H. M. Cheng, *Chem. Mater.*, 2010, **22**, 5306.
32 Z. S. Wu, W. Ren, L. Wen, L. Gao, J. Zhao, Z. Chen, G. Zhou, F. Li and H. M. Cheng, *ACS Nano*, 2010, **4**, 3187.
33 H. Wang, L. F. Cui, Y. Yang, H. S. Casalongue, J. T. Robinson, Y. Liang, Y. Cui and H. Dai, *J. Am. Chem. Soc.*, 2010, **132**, 13978.
34 N. Li, G. Liu, C. Zhen, F. Li, L. Zhang and H. M. Cheng, *Adv. Funct. Mater.*, 2011, **21**, 1717.
35 J. P. Liu, Y. Y. Li, X. T. Huang, R. M. Ding, Y. Y. Hu, J. Jiang and L. Liao, *J. Mater. Chem.*, 2009, **19**, 1859.
36 F. Shao, J. Sun, L. Gao, S. W. Yang and J. Q. Luo, *J. Phys. Chem.C*, 2011, **115**, 1819.
37 J. Jiang, J. P. Liu, X. T. Huang, Y. Y. Li, R. M. Ding, X. X. Ji, Y. Y. Hu, Q. B. Chi and Z. H. Zhu, *Cryst. Growth Des.*, 2010, **10**, 70.
38 W. S. Hummers and R. E. Offeman, *J. Am. Chem. Soc.*, 1958, **80**, 1339.
39 W. W. Zhou, J. X. Zhu, C. W. Cheng, J. P. Liu, H. P. Yang, C. X. Cong, C. Guan, X. T. Jia, H. J. Fan, Q. Y. Yan, C. M. Li and T. Yu, *Energy Environ. Sci.*, 2011, **4**, 4954.
40 F. F. Cao, X. L. Wu, S. Xin, Y. G. Guo and L. J. Wan, *J. Phys. Chem. C*, 2010, **114**, 10308.
41 Y. T. Zhong, X. Wang, K. C. Jiang, J. Y. Zheng, Y. G. Guo, Y. Ma and J. N. Yao, *J. Mater. Chem.*, 2011, **21**, 17998.
42 M. Noh, Y. Kwon, H. Lee, J. Cho, Y. Kim and M. G. Kim, *Chem. Mater.*, 2005, **17**, 1926.
43 S. Sun, F. Jaouen and J. P. Dodelet, *Adv. Mater.*, 2008, **20**, 3900.
44 T. Yu, Y. Zhu, X. Xu, K. S. Yeong, Z. Shen, P. Chen, C. T. Lim, J. T. L. Thong and C. H. Sow, *Small*, 2006, **2**, 80.
45 D. Zhao, Y. Y. Fu, Q. Han, Y. Y. Xu and H. Zhang, *J. Phys. Chem. C*, 2007, **111**, 18475.
46 L. Tang, Y. Wang, Y. Li, H. Feng, J. Lu and J. Li, *Adv. Funct. Mater.*, 2009, **19**, 2782.
47 G. Bhargava, I. Gouzman, C. M. Chun, T. A. Ramanarayanan and S. L. Bernasek, *Appl. Surf. Sci.*, 2007, **253**, 4322.
48 T. Yamashita and P. Hayes, *Appl. Surf. Sci.*, 2008, **254**, 2441.
49 G. K. Pradhan and K. M. Parida, *ACS Appl. Mater. Interfaces*, 2011, **3**, 317.
50 Y. S. Luo, J. S. Luo, J. Jiang, W. W. Zhou, H. P. Yang, X. Y. Qi, H. Zhang, H. J. Fan, D. Y. W. Yu, C. M. Li and T. Yu, *Energy Environ. Sci.*, 2012, **5**, 6559.
51 T. J. Chuang, C. R. Brundle and D. W. Rice, *Surf. Sci.*, 1976, **59**, 413.

52 M. A. Langell, M. D. Anderson, G. A. Carson, L. Peng and S. Smith, *Phys. Rev. B: Condens. Matter*, 1999, **59**, 4791.
53 M. A. Reddy, M. S. Kishore, V. Pralong, V. Caignaert, U. V. Varadaraju and B. Raveau, *Electrochem. Commun.*, 2006, **8**, 1299.
54 G. Sudant, E. Baudrin, D. Larcher and J. M. Tarascon, *J. Mater. Chem.*, 2005, **15**, 1263.
55 C. H. Jiang, M. D. Wei, Z. M. Qi, T. Kudo, I. Honma and H. S. Zhou, *J. Power Sources*, 2007, **166**, 239.
56 P. Poizot, S. Laruelle, S. Grugeon, L. Dupont and J. M. Tarascon, *J. Power Sources*, 2001, **97**, 235.
57 M. M. Rahman, J. Z. Wang, X. L. Deng, Y. Li and H. K. Liu, *Electrochim. Acta*, 2009, **55**, 504.
58 Z. Y. Wang, D. Y. Luan, S. Madhavi, Y. Hu and X. W. Lou, *Energy Environ. Sci.*, 2012, **5**, 5252.
59 X. F. Li, X. B. Meng, J. Liu, D. S. Geng and Y. Zhang, *Adv. Funct. Mater.*, 2012, **22**, 1647.
60 X. W. Lou, J. S. Chen, P. Chen and L. A. Archer, *Chem. Mater.*, 2009, **21**, 2868.
61 Y. X. Chen, L. H. He, P. J. Shang, Q. L. Tang, Z. Q. Liu, H. B. Liu and L. P. Zhou, *J. Mater. Sci. Technol.*, 2011, **27**, 41.
62 S. M. Paek, E. J. Yoo and I. Honma, *Nano Lett.*, 2009, **9**, 72.
63 N. Du, H. Zhang, B. Chen, J. Wu, X. Ma, Z. Liu, Y. Zhang, D. Yang, X. Huang and J. Tu, *Adv. Mater.*, 2007, **19**, 4505.
64 P. Poizot, S. Larunelle, S. Grugeon and M. J. Tarascon, *J. Electrochem. Soc.*, 2002, **149**, A1212.
65 S. K. Martha, J. Grinblat, O. Haik, E. Zinigrad, T. Drezen, J. H. Miners, I. Exnar, A. Kay, B. Markovsky and D. Aurbach, *Angew. Chem., Int. Ed.*, 2009, **48**, 8559.